Journal of Hazardous Materials, 11 (1985) 155—178
Elsevier Science Publishers B.V., Amsterdam — Printed in The Netherlands

DETERMINATION OF CLOUD AREA AND PATH FROM VISUAL AND CONCENTRATION RECORDS

P.W.M. BRIGHTON, A.J. PRINCE and D.M. WEBBER

Safety and Reliability Directorate, UKAEA, Wigshaw Lane, Culcheth, Warrington, Cheshire WA3 4NE (Great Britain)

(Received May 10, 1984; accepted September 15, 1984)

Summary

The area and position of the cloud are determined by two methods for each of the trials without obstructions performed at Thorney Island. In the first they are measured from photographs. The results show that the cloud area follows a closely linear variation with time, after a brief acceleration. This strongly supports the front velocity condition used in many box models of heavy gas dispersion. In the second method, applicable to much greater times, we first find the cloud envelope which bounds the area over which gas passed. A geometrical construction allows estimation of the position and size of the cloud as its boundary crosses a given point. Arrival and departure times found from concentration records are used to relate cloud geometry to time. This method, although of limited precision, indicates that the area continues to follow a similar gravity-spreading behaviour, with some influence of atmospheric turbulent diffusion. Also the clouds become somewhat elongated.

1. Introduction

All those who are concerned with studying the Thorney Island data will be guided by their own particular objectives in choosing which aspects to analyse and which methods to use. In the work described in this and an accompanying paper [1], we aim to extract from the Phase I data that information needed to assess the validity of integral models of instantaneous heavy gas cloud releases (commonly known as "box models"), such as SRD's model DENZ [2]. A large number of such models has been proposed, but a recent review of their physical bases [3] shows that many of them differ only slightly in the relations used for the turbulent processes of edge and top entrainment and, for isothermal releases, can be solved analytically in a common form. In box models the cloud is represented as a circular cylinder involving four main variables: the radius (or equivalently the area), the distance of the centre from the source, a spatially-averaged concentration and the height of the cylinder (which can be obtained from the first three by mass conservation of the released gas). These variables are all functions of time alone.

In this paper, we describe the estimation of the area of the cloud and the position of its centroid by two different methods. In the first, described in Section 2 below, we obtain these quantities manually from the overhead still photographs and video records taken from a helicopter. However the required information can be extracted from the visual records only for times up to 25—50 s after the release of the gas, while the gas concentration sensors continue to record the presence of gas for periods of the order of 10 minutes. In Section 3, a method is described for extending the results to later times by using the concentration records themselves. This relies on defining a "cloud envelope", the curve bounding all those points on the ground at which gas was present at some time or other. A geometrical construction is then applied to estimate the size and position of the cloud when it arrives at or departs from a particular sensor location; these times are obtained by visual inspection of the concentration records.

Both methods are illustrated by detailed results from two trials, in order to demonstrate the quality of the data and also to point out some of the practical difficulties. Those results from other trials which are available at the time of writing are summarised. Full results for all 15 Phase I heavy gas releases (Trials 5—19) are being made available [4, 5].

2. Analysis of overhead visual records

2.1 Method

A glance at the overhead photographs of the Thorney Island gas releases shows that, as in the experiments at Porton [6] and in wind-tunnel simulations [7], these clouds slump under gravity and form a sharp front so that there is no difficulty in defining the edge of the cloud — in contrast to the case of neutrally buoyant gas releases. Also the clouds generally have an outline which approximates to a circle, despite irregularities caused by the turbulent nature of the flow and by the dynamics of the release process [8].

To perform this analysis, we preferred, for the sake of greater clarity, to use overhead still photographs, which were taken with a motorised camera from the helicopter at an altitude of about 300 m. To analyse the stills, images from a developed 35 mm filmstrip were projected onto paper of A3 size. The cloud outlines were traced by hand. The runway and the bases of any identifiable sensor masts were also marked. The helicopter also carried a separate video camera system and for several trials this supplied the only available visual records (see Roebuck [9] for details of visual coverage). For these trials, a 16 mm ciné-film transcript of the video was used to project images for tracing onto paper. The drawings of cloud outlines, which were obtained at intervals between 1 and 2.5 seconds, were photocopied and the cloud shapes were cut out. The geometrical centroid was found by hanging the shapes up and marking verticals in three different orientations — this procedure gave self-consistent results within graphical accuracy. The areas of the clouds were found by weighing on a chemical balance together with pieces of known area.

For each frame a scaling factor was found by measuring distances between the bases of several pairs of instrument masts. In fact these measurements were not entirely consistent indicating some degree of distortion. Effects which could have contributed to this were non-verticality of the line of sight of the camera, and the optics both of the camera and of the projector. The discrepancies between scaling factors deduced from various combinations of the four masts nearest the cloud centroid were of the order of a few percent. An average value was used to scale up results for cloud area. The geometrical distortion will cause a difference between the centroid positions of the cut-out shapes and of the actual cloud outlines. There was also some uncertainty in finding the centroid displacement from the spill point in the early stages of the release as the smoke obscured the base of the gas container support column — its position had to be estimated from those of other masts.

2.2 Examples of results: Trials 8 and 14

In Figs. 1—3, we show results for the area and position of the cloud for Trial 8, a low wind-speed case (2.4 m/s), in which the cloud retained a near-circular form, and for Trial 14, in which the cloud is seen to undergo considerable elongation in the wind direction. Although this trial did not have the highest wind-speed of all, it does display the most elongation to be seen in the Phase I overhead views.

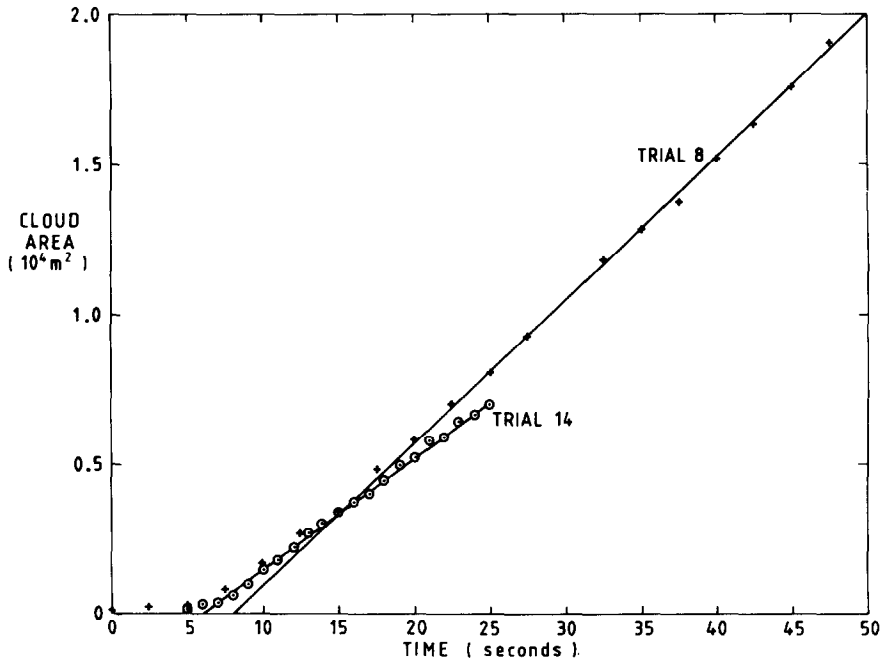

Fig. 1. Dependence of cloud area on time after release, Trials 8 and 14, as determined from photographs.

For Trial 8, the overhead stills camera was set with an interval of 2.5 s between frames. A frame showing the raising of the lid of the gas release bag was designated Frame 1 and time 0. Frame 19 was the last of the series analysed because in subsequent frames the cloud exceeded the bounds of the picture. This was also close to the point beyond which the cloud outline became too faint to trace with certainty. Figure 1 shows the cloud area as a function of time. We have taken the liberty of inserting an extra time interval between Frames 12 and 13: an obvious discontinuity in the data strongly suggests that the camera missed one shot. With this adjustment the data conform very well to a linear dependence of area on time after a short initial acceleration period. A straight line of slope 470 m^2/s has been fitted

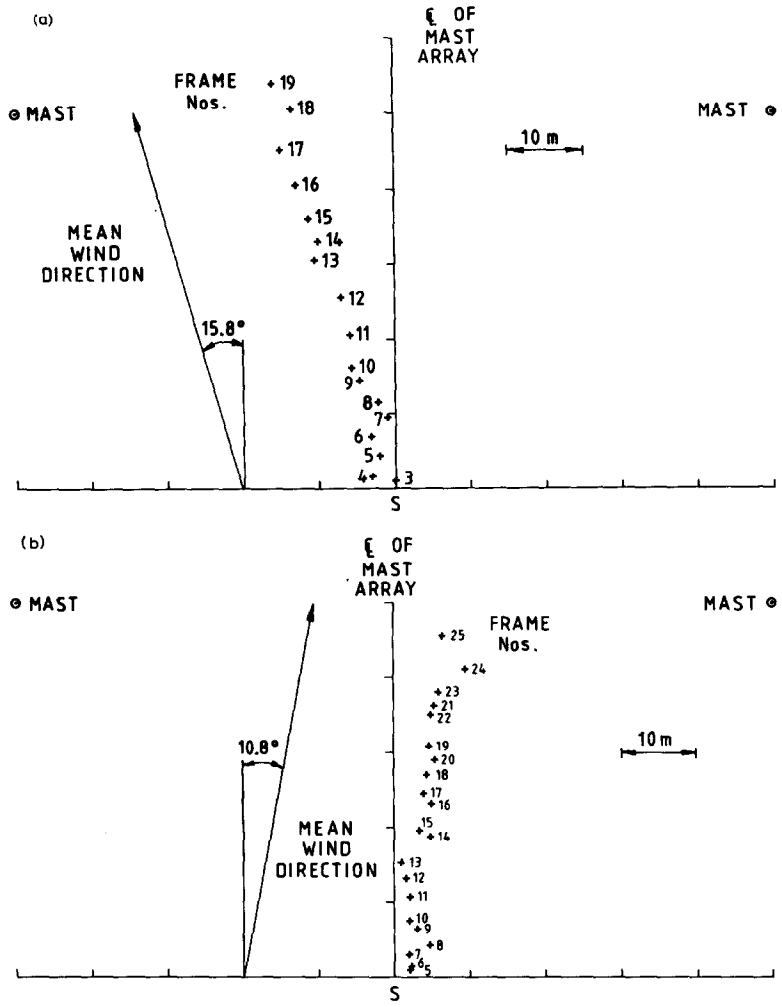

Fig. 2. Successive centroid positions determined from photographs of (a) Trial 8, (b) Trial 14.

by eye. Figure 2a shows the position of the centroid of the cloud in successive frames, referred to the fixed axes of the sensor array. As discussed above, the results are rather poor near the spill point S because the base of the support column was obscured by smoke. However, the data suffice to conclude that the cloud moves in a straight line in the direction of the mean wind. The speed of movement is more easily gauged from Fig. 3 which shows the centroid's distance from S as a function of time. The insertion of the extra time interval between Frames 12 and 13 again considerably improves the continuity of the results. The cloud displacement displays a gradual acceleration — for the last 7 frames the average speed is about 1.5 m/s.

In Trial 14 the overhead stills camera operated with a 1 s interval. With Frame 1 corresponding to the first movement of the bag lid, the analysis could be continued up to Frame 25. Although the cloud remains within the frame of the picture subsequently, the outline became invisible against the background of the white runway. Despite the irregular shape of the cloud outline, the dependence of area on time is again closely linear (Fig. 1). Figure 2b shows successive positions of the centroid giving an overall direction of movement close to that of the wind. However the centroid appears to move backwards between Frames 19 and 20 and to jump forward more rapidly than expected between Frames 20 and 21. This reflects a wispy appearance of the downwind edge of the cloud which altered the outline shape markedly from frame to frame. Figure 3 shows the centroid displace-

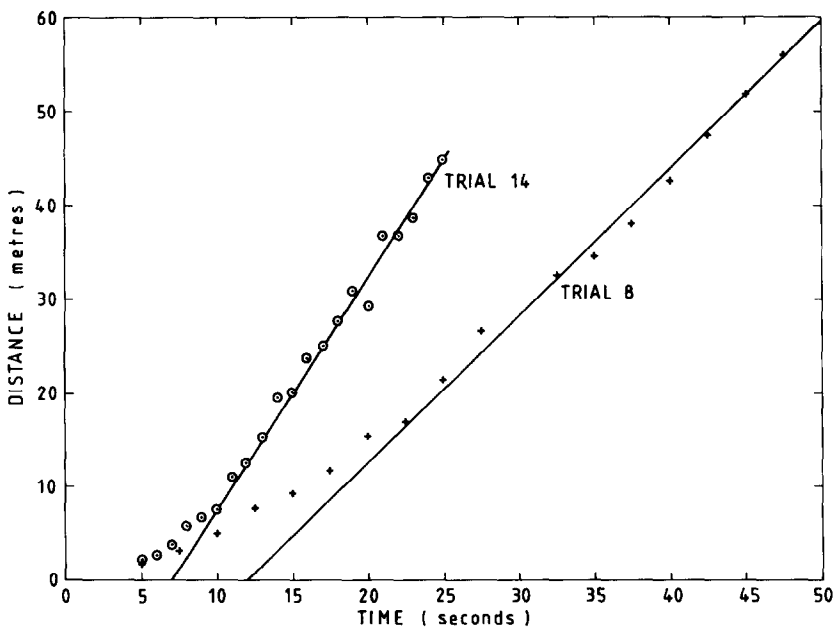

Fig. 3. Dependence of distance of centroid from source on time after release, Trials 8 and 14, as determined from photographs.

ment as a function of time: after an initial acceleration lasting about 10 s a fairly constant speed of about 2.5 m/s is maintained for the remaining 15 s covered by the analysis.

2.3 The gravity-spreading law

The results reported in Section 2.2 and Figs. 1—3 are intended to be representative of the quality of all the results obtained. The linear relationship between area and time was found to apply equally well to the other Phase I trials and so the results can be summarised adequately by the constant values of area increase rate. These are listed in Table 1 together with the estimates of cloud speed which again, as in Fig. 3, was always fairly constant after an initial acceleration period. Graphs of area and centroid position are given in full in [4].

In Table 1, the initial density ratio and volume of the released gas are also given so that the area increase rate can be converted to a dimensionless Froude number, K. The significance of this quantity can be seen by considering an equation for the speed of the propagating gravity current head which forms the edge of these clouds. This equation is common to many of the box models of heavy gas dispersion [3]:

$$U_F = dR/dt = K\sqrt{g\Delta' h}. \quad (1)$$

TABLE 1

Area increase results from overhead photographs Phase I

Trial No.	Wind speed (m/s)	Cloud speed (m/s)	Density ratio, ρ_0/ρ_A	Initial volume (m^3)	Cloud area increase rate (m^2/s)	Froude No., K
5	4.6	4.28	1.69	2000	500	1.2[a]
6	2.6	1.4	1.60 ± 6%	1580 ± 7%	292	0.85 ± 0.10[b]
7	3.2	1.39	1.75 ± 6%	2000 ± 5%	418	0.97 ± 0.10
8	2.4	1.49	1.63 ± 6%	2000 ± 5%	470	1.19 ± 0.12
9	1.7	0.77	1.60 ± 8%	2000 ± 5%	480	1.25 ± 0.16
10	2.4	1.06	1.80 ± 15%	2000 ± 5%	495	1.12 ± 0.21
11	5.1	1.57	1.96 ± 4%	2100 ± 5%	458	0.92 ± 0.06[c]
12	2.6	—	2.37 ± 3%	1950 ± 5%	No overhead photographs	
13	7.5	2.89	2.00 ± 2%	1950 ± 5%	517	1.06 ± 0.06[b]
14	6.8	2.49	1.76 ± 6%	2000 ± 5%	375	0.87 ± 0.08
15	5.4	2.36	1.41 ± 7%	2100 ± 7%	325	1.00 ± 0.16
16	4.8	1.80	1.68 ± 5%	1580 ± 7%	389	1.07 ± 0.11
17	5.0	2.20	4.20 ± 0%	1700 ± 5%	617	0.75 ± 0.02[b]
18	7.4	3.41	1.87 ± 5%	1700 ± 5%	465	1.02 ± 0.09[c]
19	6.4	2.18	2.12 ± 4%	2100 ± 5%	567	1.05 ± 0.06[c]

[a]Container fell in two stages.
[b]Significant portion of cloud not visible against runway.
[c]A small portion of cloud not visible against runway.

Here U_F is the front speed, R the cloud radius and t time. g is the acceleration due to gravity and h is the cloud height while $\Delta' = \rho/\rho_A - 1$ where ρ is the density of the cloud and ρ_A is the density of the ambient air. The Froude number, K, is assumed to be a constant near 1. Equation (1) leads to an equation for the cloud area $A = \pi R^2$:

$$dA/dt = 2\pi R dR/dt = 2\pi K b^{\frac{1}{2}} \tag{2}$$

where

$$b = g\Delta' V/\pi \tag{3}$$

and V is the cloud volume. b, the total buoyancy in the cloud, remains constant throughout the release for isothermal conditions (as at Thorney Island) and in certain other circumstances [3]. Hence (2) can be integrated to yield a linear dependence of area on time. The Froude number can be obtained from the area increase rate and the initial conditions of the release as

$$K = \frac{dA/dt}{2\sqrt{\pi g \Delta_0' V_0}} \tag{4}$$

where subscript 0 denotes initial values.

Equation (4) produces the values listed in the last column of Table 1. Table 1 gives a range of uncertainty for K caused by the uncertainties indicated in the values of initial density ratio and volume. These ranges for the initial conditions were estimated by NMI Ltd. by comparing the various means of monitoring the process of filling the gas bag. In three of the trials (Nos. 6, 13 and 17) a significant proportion of the cloud was not visible against the white runway. In Trial 5, the gas bag stuck during its descent and also only 3 frames were of sufficient quality for tracing cloud outlines. Of the remaining 10 trials, a few suffered slightly from invisibility on the runway but this affected the area values by less than 5%, judging by a mental extrapolation of the cloud outlines. For these 10 trials the mean value of the Froude number is

$$\bar{K} = 1.05 \tag{5}$$

with a standard deviation (based purely on the central values for K in Table 1) of 0.12. This standard deviation is probably accounted for by the uncertainty in initial conditions together with various sources of measurement error in the areas.

This value of the frontal Froude number compares with a value of 0.89 which can be obtained from van Ulden's [10] model of an experiment involving the rapid spillage of 1 tonne of liquid Freon 12 and a value of 1.08 ± 0.25 obtained from our own analysis [4] of 13 of the Porton trials. (This analysis required establishing criteria for selecting points from the area—time graphs relevant to gravity spreading — in many of the trials there was no such period free from the influences either of the initial acceleration or of passive turbulent diffusion.)

On the hypothesis that these clouds slump in a self-similar manner, the spreading law (1) can be regarded as the only possibility on dimensional grounds, apart from a possible variation of K with the density difference ratio Δ' which during these releases declines from a value near 1 down to values near 0 as the cloud is diluted with air. The linearity of the present results thus confirms that K is independent of Δ' over this range of densities. This is consistent with physical interpretation of eqn. (1) as representing a balance between the hydrostatic driving force of the gravity current head, $\frac{1}{2}(\rho - \rho_A)gh^2$, and the aerodynamic drag due to the displaced air, $C_D\rho_A U_F^2 h$ where C_D is a drag coefficient of order 1. In contrast to this, as noted in [3], some modellers have used $\Delta = (\rho - \rho_A)/\rho = \rho_A\Delta'/\rho$ instead of Δ' in the front condition (1).

2.4 The speed of translation of the cloud

In Table 1, the ratio of the mean cloud speed (as determined from graphs such as Fig. 3) to the mean wind speed at 10 m has an average value of 0.42 with a standard deviation of 0.09 for the 10 trials for which the photographic data were satisfactory. This cannot be regarded as a particularly fundamental value since the time periods for which the speed was determined are somewhat arbitrary and the clouds are probably still accelerating. Presumably the cloud accelerates mainly because of the addition of momen tum from the air entrained into it. Eventually, when it becomes diluted enough to behave as a passive contaminant, its mean translational speed will be related to the speed of the atmospheric boundary layer at the height of the centre of mass of the cloud [11, 12].

In view of these considerations we conclude that a proper analysis of these results for cloud speed must involve deriving a relation involving the cloud height, determination of which is discussed in [1], and the mean velocity profile, which we have not yet studied.

3. Use of cloud envelope and arrival and departure times

3.1 General description

During the time period covered by the photographic analysis described in Section 2, the gas cloud arrives at only 2 or 3 of the sensor masts at most, at up to 100 m from the source. In order to trace the development of the cloud up to distances of 500 m or more covered by the sensor array a different approach is needed.

The method presented here uses the arrival and departure times of the cloud at each mast. As one might expect from the overhead photographs, many of the concentration records show a sharp well-defined rise of concentration as the cloud first arrives, though at later times the front becomes more diffuse. Departure times are less well defined and this does lead to considerable uncertainty in some trials about the location of the cloud's upwind edge. This is not crucial to the method of analysis however: this starts out by

looking at the ground pattern of sensors which detected gas, irrespective of the times at which they did so. This leads to a determination of what we shall call the "cloud envelope", i.e. the curve bounding the area on the ground at which gas was present at some time. In practice, the instantaneous cloud boundary and the cloud envelope depend on the lower limit of resolution of the gas sensors, which concentration records from the trials indicate to be generally somewhat lower than 0.1%. The level of resolution probably makes little difference to the determination of the envelope because of the greater uncertainty stemming from the 100-m spacing of the sensor masts. However the resolution could have a significant effect on arrival and departure times, particularly at later stages of the releases. The shape of the envelope depends on the relation between the size of the cloud and its position, but it does not involve the dependence of these on time.

The basis of the method is to model the cloud outline as a circle whose radius is calculated as a function of the distance of the centre from the release point. For any point within the cloud envelope one can calculate the radius and position of the cloud when its edge passes through that point, i.e. at the arrival and departure times at a particular sensor location. Geometrically, this consists of finding a circle tangent to the envelope at two points and also passing through a third, prescribed point, within it (see Fig. 4).

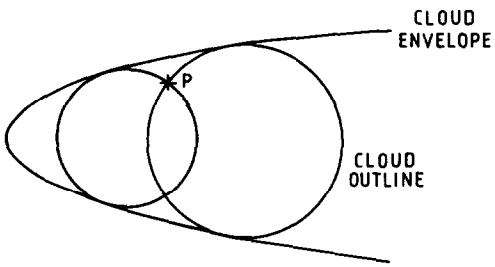

Fig. 4. Sketch illustrating determination of cloud size and position as outline passes point P.

Clearly, the irregular shape of the cloud and the lack of precision in finding the cloud envelope make this procedure somewhat approximate. What we have done is to use this geometrical model to derive a correlation for a collection of data-points in space—time (X, Y, t) known to lie on the cloud boundary. If the cloud remained perfectly circular and we found the correct cloud envelope, the resulting plots of centroid position against time would fall on smooth curves. The usefulness of the procedure can be assessed only by trying it out and judging whether the results are reasonably self-consistent. In this paper examples of detailed results are given for two trials, Nos. 7 and 9, the second of which illustrates many of the difficulties that can arise. Nevertheless we believe that these difficulties can be overcome and that useful estimates of cloud area and position can be derived. Full results for all trials are being made available in a separate publication [5].

3.2 Mathematical details: use of a composite parabolic cloud envelope and relation to cloud development

Let X and Y be the coordinates describing the ground plan of the Thorney Island experimental range. The centreline of the array of masts is parallel to the Y-axis with the release point at $(X_0, Y_0) = (4,2)$ measured in units of 100 m. Consider a circular cloud moving along a straight path at an angle θ to the Y-axis. θ increases in the anti-clockwise direction. To describe the cloud envelope we transform to coordinates (x, y) with origin at (X_0, Y_0) and with x-axis coincident with the cloud path. Thus the new coordinates are given by

$$\begin{aligned} x &= -(X - X_0)\sin\theta + (Y - Y_0)\cos\theta, \\ y &= -(X - X_0)\cos\theta - (Y - Y_0)\sin\theta. \end{aligned} \tag{6}$$

We suppose that the cloud radius $R(t)$ and the distance of its centre from the spill-point $\xi(t)$ are connected by a relationship of the form

$$R^2 = R_i^2 + p_i(\xi - \xi_i), \qquad \xi_i \leqslant \xi \leqslant \xi_{i+1}, \qquad i = 0, 1, 2, \ldots, n. \tag{7}$$

The initial point in this formula is given by the release conditions $R = R_0$ for $\xi = \xi_0$, with $R_0 = 7$ m, the container radius. The curve $R^2(\xi)$ is required to be continuous, so the coefficients p_i are given by

$$p_i = (R_{i+1}^2 - R_i^2)/(\xi_{i+1} - \xi_i). \tag{8}$$

The piecewise linear relation (7) could in principle be used to approximate an arbitrary relation between R^2 and ξ, simply by using a sufficiently large number of intervals $[\xi_i, \xi_{i+1}]$. The cloud envelope that it generates (cf. Fig. 4) consists of a succession of conjoined segments of parabolae all symmetrical about the straight cloud path. In practice, it is found that no more than three or four intervals are warranted since the accuracy is limited by the mast spacing (see Fig. 6a for examples of cloud envelopes).

Relation (7) can also be regarded as a generalisation of the result obtained for a cloud moving with constant speed whose area increases linearly with time as found in the photographic analysis of Section 2.

To determine the cloud envelope, we first consider the equation of the circular cloud outline

$$(x - \xi)^2 + y^2 = R^2. \tag{9}$$

For a given point (x, y), combining (7) and (9) leads to a quadratic equation for ξ, the centre position of the cloud when its edge passes through (x, y):

$$\xi^2 - (p_i + 2x)\xi + x^2 + y^2 - R_i^2 + p_i\xi_i = 0 \tag{10}$$

with solutions

$$\xi_\pm = x + \tfrac{1}{2}p_i \pm [p_i(x - \xi_i) - y^2 + R_i^2 + \tfrac{1}{4}p_i^2]^{\frac{1}{2}}. \tag{11}$$

The condition for (x, y) to lie on the cloud envelope is that equation (11) represents a double root:

$$p_i(x - \xi_i) = y^2 - R_i^2 - \tfrac{1}{4}p_i^2 \tag{12}$$

which is a parabola symmetric about the x-axis with apex $y = 0$ at

$$x_A = \xi_i - R_i^2/p_i - \tfrac{1}{4}p_i. \tag{13}$$

As each parabolic arc is used only for part of the cloud envelope, it is necessary to determine the points at which the joins will occur in terms of the parameters R_i and ξ_i. A circle centred at $x = \xi$, $y = 0$ with $\xi_i < \xi < \xi_{i+1}$ touches the cloud envelope at points (x, y) given by solving simultaneously eqns. (7), (9) and (12) with the results

$$x = \xi - \tfrac{1}{2}p_i, \qquad y = \pm(R^2 + \tfrac{1}{4}p_i^2)^{\frac{1}{2}}. \tag{14}$$

Let $(x_i, \pm y_i)$ be the points where sections of parabola meet corresponding to the intervals $[\xi_{i-1}, \xi_i]$ and $[\xi_i, \xi_{i+1}]$ on the cloud path. In practice, we select a set of points (x_i, y_i) to join up to form a cloud envelope and we then wish to determine the parameters ξ_i and R_i^2. First, we have from equation (8)

$$p_i = (y_{i+1}^2 - y_i^2)/(x_{i+1} - x_i). \tag{15}$$

Since $x = x_j$, $y = y_j$ satisfies eqn. (12) for both $j = i - 1$ and $j = i$, we find using eqn. (8) that ξ_i and R_i^2 are given by

$$\xi_i = x_i + \tfrac{1}{4}(p_{i-1} + p_i), \qquad R_i^2 = y_i^2 + \tfrac{1}{4}p_{i-1}p_i. \tag{16}$$

Note that when its centre is at the end of an interval $[\xi_{i-1}, \xi_i]$ the circle is not touching the join-point (x_i, y_i). If, as is the case in practice, $p_i < p_{i-1}$, then the two parabolae meet at a convex angle and at the changeover the circle is touching both parabolic arcs simultaneously (see Fig. 5). For this reason, relations (14) giving the point of tangency and (16) giving the join-point are different. Thus our composite cloud envelopes consist of parabolic arcs joined by circular ones — in practice the circular parts are relatively short.

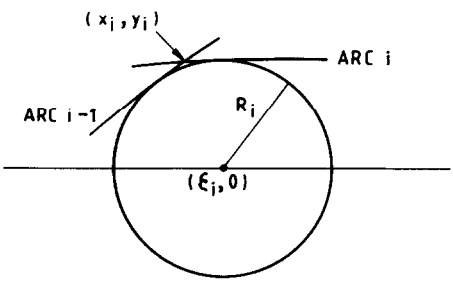

Fig. 5. Changeover between parabolic arcs.

In applying this geometrical model to describing actual cloud envelopes, a set of points (x_i, y_i) on the envelope are specified initially and (15) and (16) are used to calculate the parameters in the $R^2 - \xi$ relationship (7). For the first interval, $0 \leqslant \xi \leqslant \xi_1$, R_1^2 and ξ_1 can be obtained directly from the analysis of the photographs by Prince et al. [4].

3.3 Examples of results: Trials 7 and 9

The first part of the procedure is the determination of a range of possible cloud envelopes. Figure 6a shows a plan of part of the sensor array indicating those sensors which detected gas during Trial 7. The problem here is to find a reasonably smooth curve to separate these sensors from those which did

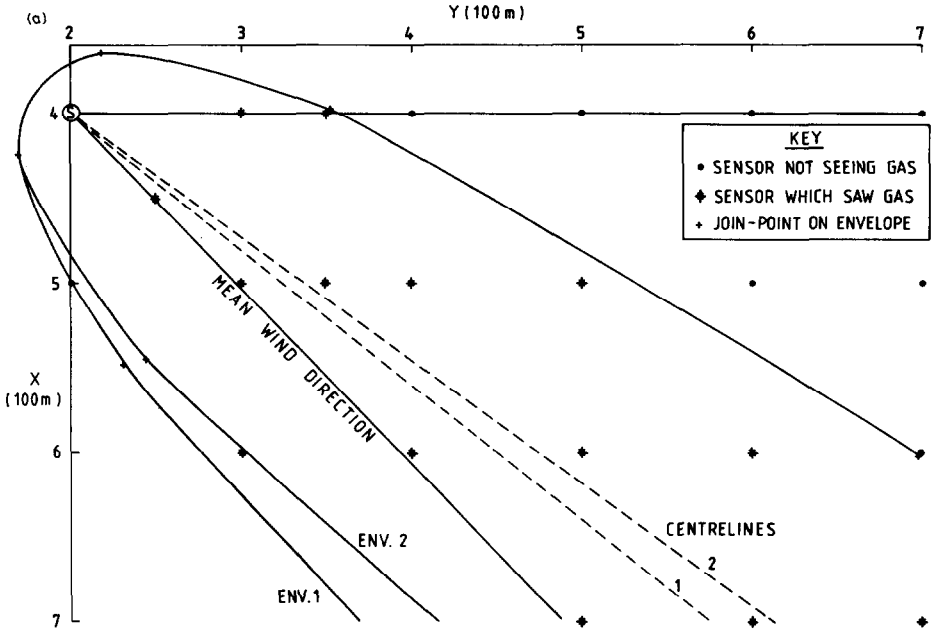

Fig. 6a. Cloud envelopes for Trial 7.

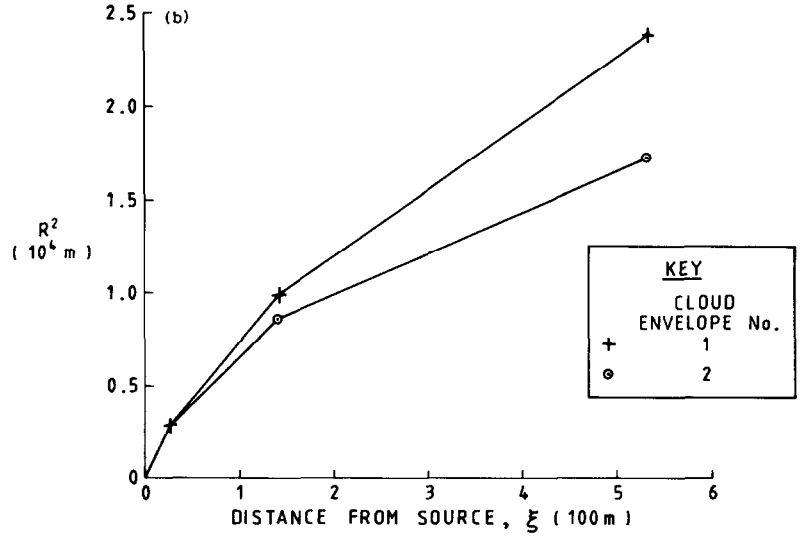

Fig. 6b. R^2—ξ relationships for cloud envelopes, Trial 7.

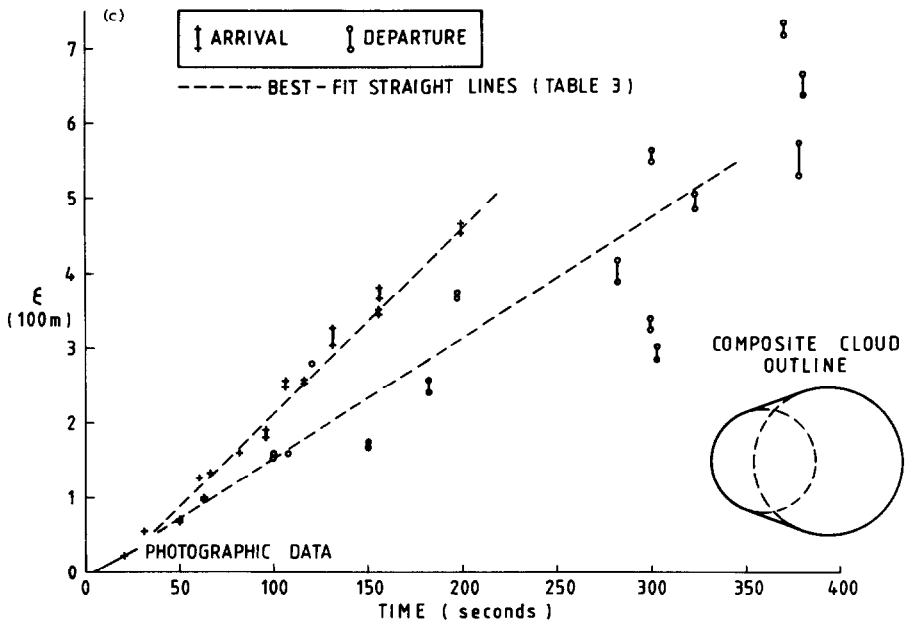

Fig. 6c. Apparent cloud centre displacements, Trial 7.

not detect gas — this involves choosing a direction of cloud motion θ and then a selection of join-points for the composite parabola described in Section 3.2. There is of course no unique solution to this problem and there is no obvious way to define an optimum. Even the task of finding any curve satisfying all the constraints would be rather complex to program for a computer. Instead the sets of join-points defining each envelope has been judged by eye so as to steer a smooth course between the two groups of sensors — in most cases it is just a few critical sensors positioned near the envelope which guide the decisions.

At first sight the disposition of sensors detecting gas during Trial 7 is unfavourable because on the right-hand side of the cloud path (looking downwind) only the sensor at (5,2) did not detect gas (see Fig. 6a). However it happens that the left-hand side of the envelope is fixed within fairly narrow limits by the requirements of passing outside (4,3.5) and inside (6,7). Our results for cloud area and position [4] have been used to determine the first section of the R^2—ξ curve in Fig. 6b and thus the cloud envelope shape near its apex. With the left-hand side fixed and the near-source portion of the right-hand side forced to pass between (5,2) and (6,3), only a limited range of cloud paths are possible and the symmetry then determines the position of the right-hand side of the envelope even though the cloud edge has strayed beyond the confines of the instrument array. In view of these considerations, only two cloud envelopes have been considered as shown in Fig. 6a. In fact, envelope No. 2 takes the cloud direction slightly too far to the left and the sensor at (6,3) falls outside. Note that in arriving at these cloud envelopes,

we have relied on assuming that the cloud path remains straight throughout the release. The resulting direction agrees with the results in [4] but is about 10° to the left of the mean wind heading given in the summary of conditions for the trial contained in the volume of hard copy plots issued by HSE [9]. However the graphical wind heading data suggest that the direction during the first 200 s after release was much nearer this range of cloud path directions estimated from the cloud envelope.

Figure 6c shows the results of calculating $\xi_\pm$ from eqn. (11) for each of the masts detecting gas and plotting the results for ξ_- against the corresponding arrival times and for ξ_+ against the departure times as determined from visual inspection of the concentration records. The section number i is chosen so that $\xi_\pm$ each lie in the correct interval $[\xi_i, \xi_{i+1}]$, which may differ for the two roots. Full lists of the time values used are given in [5]. In Fig. 6c two values are shown for each time value, corresponding to the two envelopes of Fig. 6a. The values of ξ_- for arrival exhibit an encouragingly consistent trend and the ranges produced are fairly small compared to the total distance moved. They can be correlated very well by a straight line. That shown in Fig. 6c has been fitted by the least-squares technique to the results of using envelope No. 1 of Fig. 6a. Also shown in Fig. 6c is the graph of centroid position against time from the photographic analysis [4] showing a reasonable consistency between the two methods.

A few of the departure results fall in with the trend of the arrival times but the rest lag behind by varying amounts up to 200 s. This indicates a breakdown of the assumption of near-circularity with the cloud adopting an elongated shape. This does not invalidate the present analysis because the different values of ξ for front and rear can be regarded as representing centres of curvature of the front and rear of the cloud, rather than the centroid of the whole cloud. The cloud is now represented by the area enclosed by two circles and their common tangents as indicated in the inset sketch in Fig. 6c. Despite the scatter of the departure time results, it is useful to find the line giving the least-squares best fit in order that estimates of the cloud's area may be made, as discussed in the following section.

Figure 7a shows the pattern of sensors detecting gas in Trial 9, which had the lowest windspeed in Phase I. As a result the cloud spreads very wide under gravity without being displaced very far. The envelope is therefore very wide, but determination of it is hampered by a complete lack of sensors *not* detecting gas to the left of the cloud path. On the right-hand side the envelope is determined by the need to pass outside (5,2) and (5,4) but then it is impossible to stay inside (4,5) without leaving (3,6) outside the envelope. Hence the non-response at (4,5) has been ignored. Taking the mean wind direction as the centreline of the envelope then results in an envelope which narrows in the latter stages (see Fig. 7b), even when taking the envelope as far to the right as possible while staying inside (3,7). A second, wider envelope has been generated by taking the centreline about 5° to the left of the mean wind direction. Since the real cloud presumably does not contract in

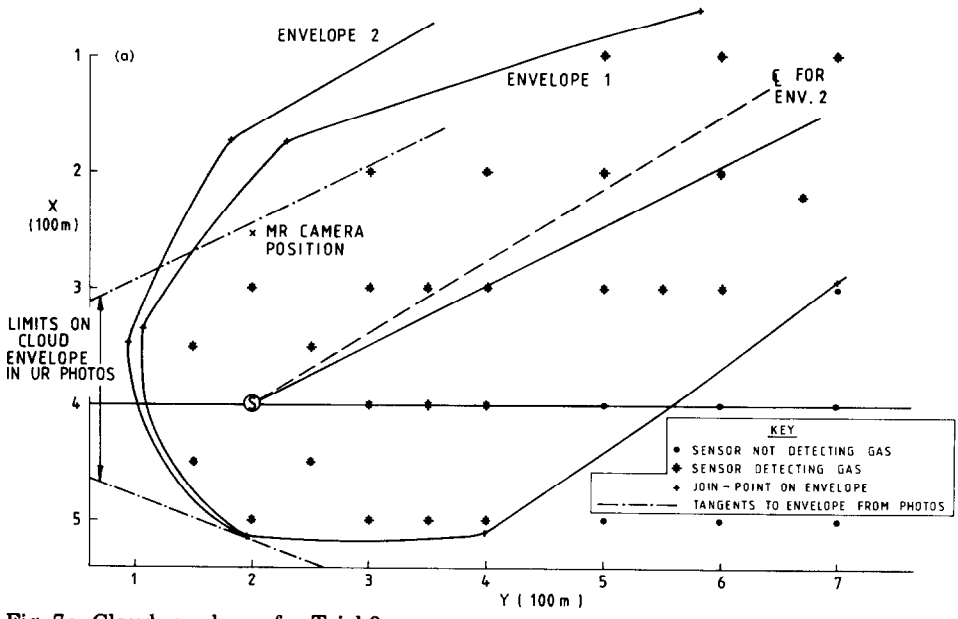

Fig. 7a. Cloud envelopes for Trial 9.

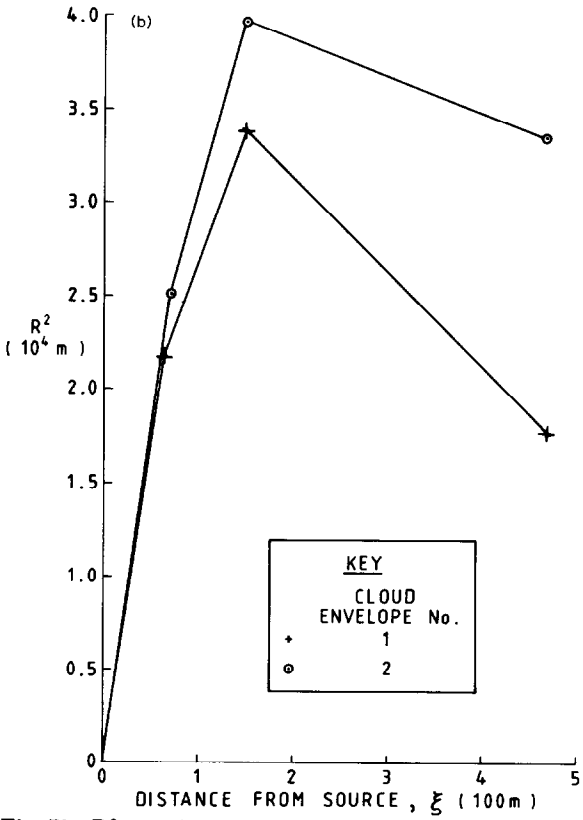

Fig. 7b. R^2—ξ relationships for cloud envelopes, Trial 9.

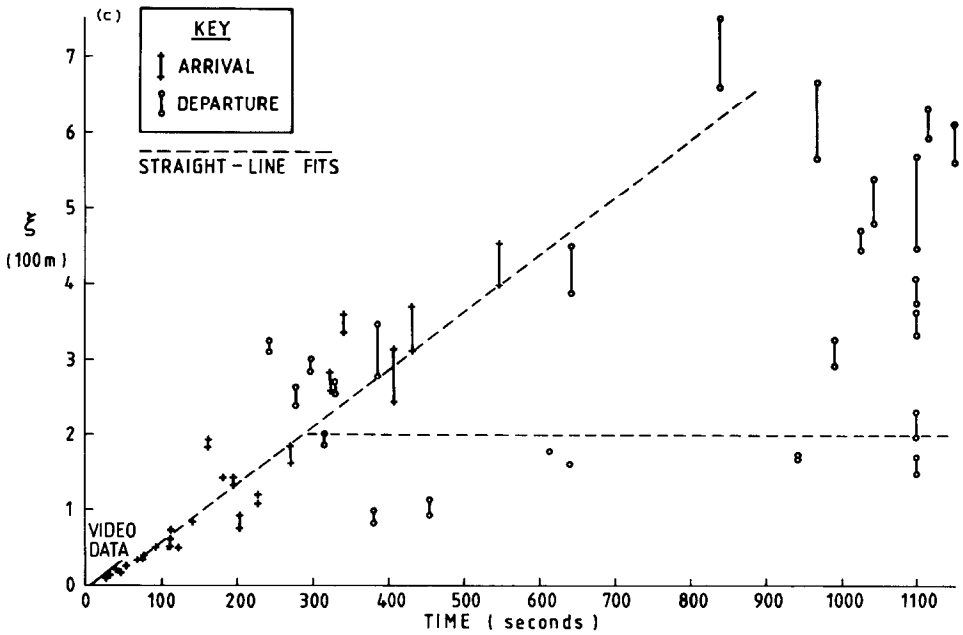

Fig. 7c. Apparent cloud centre displacements, Trial 9.

this way, this phenomenon must represent the effect of the lower limit of resolution of the sensors so that we are in fact estimating the envelope of points at which concentrations exceed the lower limit of resolution of the sensors. Trial 9 is unique in yielding cloud envelopes that narrow in this manner.

Proceeding with the calculations of $\xi_{\pm}$ for the front and rear of the cloud produces the results shown in Fig. 7c. The arrival time results show considerably more scatter than in Trial 7 but they are still fairly well described by fitting a straight line. The departure times are quite erratic — some are near the arrival time data implying a near-circular cloud, but others are extremely large — in fact many of the sensors were still detecting at the end of the period of collection of data at about 1100 s after the release. Two related factors perhaps account for these results. First, many of the gas sensors displayed erratic behaviour, making determination both of arrival and departure times difficult. This may well be due to the high humidity on this fine autumn evening (see [13] for the effects of humidity on gas sensors). This humidity also caused condensation on the smoke particles so that the orange cloud appeared to be transformed to a white low-lying mist. The second factor was that this mist persisted for several hours around the spill-point, suggesting that gas remained almost stagnant near the ground, which could be interpreted as meaning that the upwind edge of the cloud remained practically stationary during the trial. To take account of these factors, it was judged appropriate to represent the position of the centre of curvature

of the upwind edge by a constant value as shown in Fig. 7c. This value is used to calculate the cloud area given below.

These two trials serve to exemplify the kind of results obtained using this method. While some trials yielded better results than Trial 7, as regards definition of the upwind edge, none proved more difficult to analyse than Trial 9. Full results are given in [5].

3.4 Summary of results and calculation of cloud areas

The results obtained for other trials by determining cloud envelopes and using arrival and departure times to estimate the motion of the cloud are summarised in Tables 2 and 3.

In Table 2 we give the parameters ξ_i and R_i^2 which define the cloud envelope for each trial via eqns. (8) and (12). Usually there is a range of possible envelopes: one has been selected to give the best results for the cloud mass balance, whose calculation is described in [1]. Table 3 gives the equations of the straight lines fitted to the results of calculating $\xi_\pm$ for all the relevant sensor masts and plotting them against the arrival and departure times. A comprehensive report [5] illustrates all the envelopes studied and tabulates the arrival and departure times used, as well as giving the plots of $\xi_\pm$ against time.

TABLE 2

Parameters defining cloud envelopes

Trial No.	Centreline direction, θ [c] (degrees)	Values of distance from source, ξ [a], and square of cloud radius, R [b], used to generate envelope							
		ξ_1	R_1^2	ξ_2	R_2^2	ξ_3	R_3^2	ξ_4	R_4^2
5	[d]								
6	[d]								
7	−38.66	0.312	0.292	1.421	0.988	5.329	2.384	—	—
8	11.97	0.560	0.606	2.667	2.527	5.696	3.540	—	—
9	33.02	0.700	2.517	1.488	3.961	4.680	3.350	—	—
10	−140.00	0.306	0.545	—	—	—	—	—	—
11	−69.60	0.636	0.612	1.766	1.371	—	—	—	—
12	−45.00	0.711	2.812	1.230	3.871	2.540	5.787	4.739	7.346
13	−23.96	0.382	0.231	1.927	0.629	5.056	1.197	—	—
14	−4.04	1.789	0.733	5.070	1.711	—	—	—	—
15	−0.57	0.674	0.321	4.113	1.031	—	—	—	—
16	5.71	0.693	0.476	2.251	1.009	5.266	1.686	—	—
17	−45.00	1.011	0.804	2.968	1.634	5.724	2.005	—	—
18	−12.91	1.076	0.435	3.637	1.612	5.842	3.026	—	—
19	−35.54	0.197	0.149	1.046	0.471	4.251	2.077	—	—

[a] Unit 100 m.

[b] Unit 10^4 m^2.

[c] Note that the sign convention for θ is opposite to that adopted by NMI in describing wind heading.

[d] Results not available at time of writing.

In Table 3 we also list values of the speed of the apparent centre of the downwind cloud edge $\dot{\xi}_- \equiv d\xi_-/dt$ as fractions of the mean windspeed at 10 metres, $\bar{U}_{10}$. In several cases the speed is about the same as the centroid speed determined from photographs for the early stages, these values being repeated in Table 3 as fractions of $\bar{U}_{10}$. In other cases it is considerably larger but the average is not much greater than $\frac{1}{2}\bar{U}_{10}$. It should be noted that this speed is no longer the same as the speed of the cloud centroid, still less the same as the speed of the cloud's centre of mass. As the concentration distribution in the cloud may have become non-symmetrical in the wind direction, there seems no justification for carrying out the somewhat complex calculations to find the centroid of our geometrical model of the cloud outline. In some cases in Table 3 the speed of the upwind centre of curvature actually emerges as slightly greater than the speed of the downwind centre. However, during the time period covered by the data, the upwind centre never actually overtakes the downwind centre. This simply reflects the uncertainties in fitting a line through the much more scattered departure time data. Most of these trials were in high windspeeds promoting rapid dilution, so a reason for the effect may be that the later departure times were underestimated because concentrations had fallen below the sensitivity limit of the gas sensors. As remarked in Section 2.4, interpretation of the cloud speeds awaits an analysis of the mean velocity profiles.

In Figs. 8 and 9 we present the results of calculating the areas of the clouds and of their width-to-length ratios, using the correlations of Table 3

TABLE 3

Correlations for distances from source of apparent centres of downwind and upwind edges of cloud

Trial No.	Apparent centre based on arrival times, ξ_- (units 100 m and 100 s)	Apparent centre based on departure times, ξ_+ (units 100 m and 100 s)	$\dot{\xi}_-/\bar{U}_{10}$	$\dot{\xi}/\bar{U}_{10}$ (from Table 1)
5	[a]			(0.93)
6	[a]			(0.54)
7	$2.51t - 0.38$	$1.62t - 0.11$	0.78	(0.43)
8	$1.48t - 0.11$	$1.55t - 0.60$	0.62	(0.62)
9	$0.76t - 0.19$	2.00	0.45	(0.45)
10	$1.06t - 0.08$	$1.06t - 0.08$	0.44	(0.44)
11	$2.24t - 0.10$	$2.19t - 0.09$	0.44	(0.31)
12	$0.78t - 0.10$	$0.49t + 0.90$	0.30	—
13	$4.85t - 0.25$	$3.91t - 0.49$	0.65	(0.39)
14	$4.51t - 0.67$	$4.55t - 1.77$	0.66	(0.37)
15	$4.29t - 0.48$	$4.47t - 1.48$	0.80	(0.44)
16	$2.72t - 0.15$	$3.08t - 1.19$	0.57	(0.38)
17	$2.50t - 0.09$	$1.08t - 0.27$	0.50	(0.44)
18	$5.67t - 0.36$	$6.94t - 2.30$	0.77	(0.46)
19	$3.58t - 0.20$	$4.02t - 2.32$	0.56	(0.34)

[a]Results not available at time of writing.

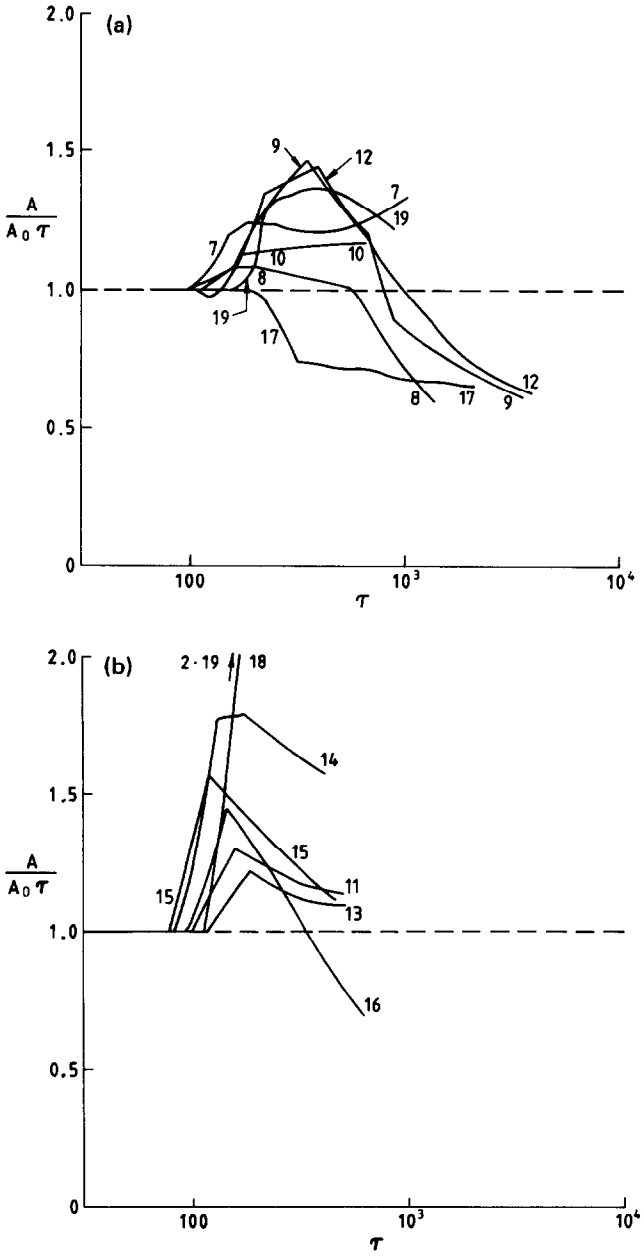

Fig. 8. Graphs of ratio of cloud area as determined by cloud envelope analysis to area expected from gravity-spreading law. Trial numbers as indicated on graphs. (a) High-Ri_0 trials, (b) low-Ri_0 trials.

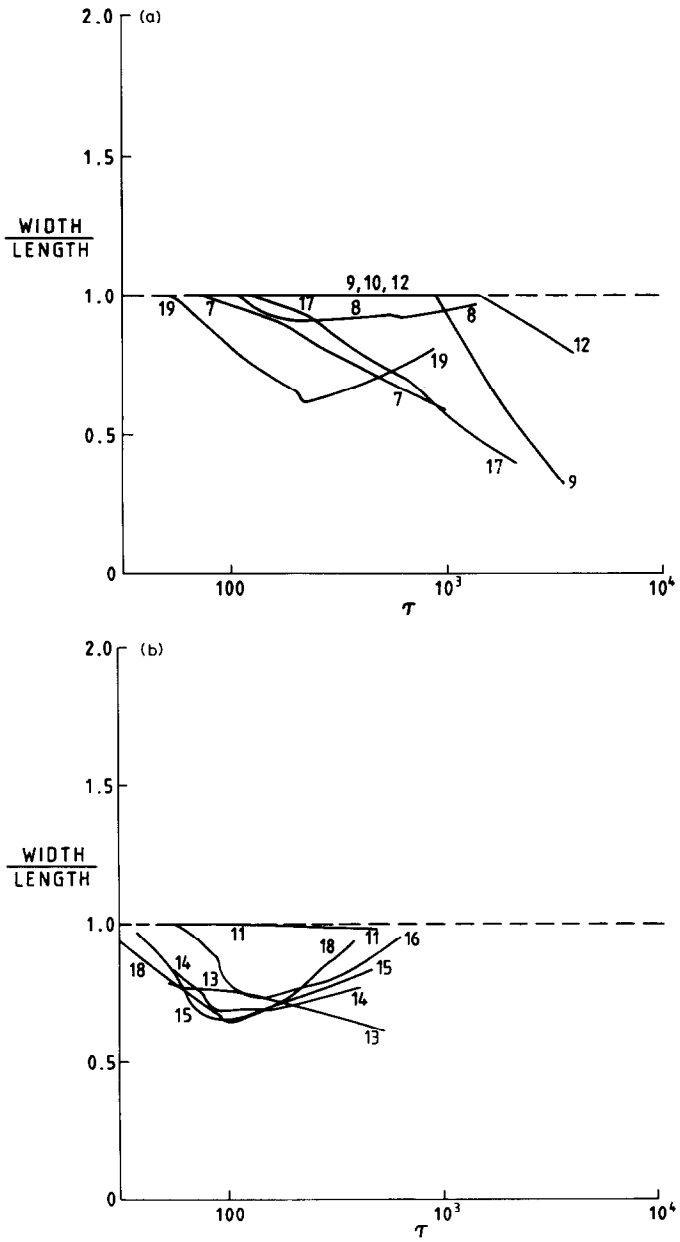

Fig. 9. Graphs of ratio of cloud width to length, as determined by cloud envelope analysis. Trial numbers as indicated on graphs. (a) High-Ri_0 trials, (b) low-Ri_0 trials.

for ξ_- and ξ_+. With the two-circle cloud shape shown in the inset in Fig. 6c, the cloud area is estimated as

$$A = \tfrac{1}{2}(\pi + 2\alpha)R_-^2 + \tfrac{1}{2}(\pi - 2\alpha)R_+^2 + (R_- + R_+)(\xi_- - \xi_+)\cos\alpha \qquad (16)$$

with

$$\alpha = \sin^{-1}((R_- - R_+)/(\xi_- - \xi_+)).$$

Here $R_\pm$ are calculated from $\xi_\pm$ according to eqn. (7), i.e. by interpolation between the parameter values given in Table 2. The formula has been used to calculate areas only after 60 s after release in each trial. For 0—40 s, the area obtained from photographs has been used and for 40—60 s a linear combination of the two results has been used so as to maintain continuity of the area. The width-to-length ratio is simply

$$2R_-/(R_- + R_+ + \xi_- - \xi_+). \tag{17}$$

A logarithmic scale of dimensionless time, τ, has been used in Figs. 8 and 9 in order to facilitate direct comparison with graphs given in [1]. This time is defined by

$$\tau = (t - t_1)/\mathcal{T} \tag{18}$$

with

$$\mathcal{T} = R_0^2/2Kb^{\frac{1}{2}} = \pi R_0^2/(\mathrm{d}A/\mathrm{d}t),$$

where t_1 is the effective time origin for the linear growth law of area shown in Fig. 1 and $\mathcal{T}$ is the time for the area to increase by an amount equal to the initial area $A_0 = \pi R_0^2$. The equality of the two expressions for $\mathcal{T}$ comes from the gravity-spreading law (2). The usefulness of this time-scale is discussed in [1], where values of t_1 and $\mathcal{T}$ are tabulated for all the Phase I trials.

In Fig. 8 we have plotted $A/A_0\tau$ to show clearly *deviations* of the area as estimated from the results in this Section from the area expected according to the gravity-spreading law $A/A_0\tau = 1$. The results have been divided into two groups in Figs. 8 and 9 for clarity of presentation: the groups are based on values of the initial Richardson number Ri_0 as defined and tabulated in [1]. The values of $A/A_0\tau$ for the high-Ri_0 cases (Fig. 8a) tend to increase somewhat above unity and then decrease, presumably because of the effects of instrument sensitivity. The spread of the results is probably representative of their general accuracy because of the uncertainty of the cloud envelope shapes and the scatter of arrival and departure times. In the low-Ri_0 cases (Fig. 8b) the data are available for a shorter period because the windspeed is generally higher and so the cloud is advected through the instrument array more rapidly. For several of these trials the behaviour is generally similar to that in Fig. 8a, but Trials 14 and 18 give results that begin to look significantly higher than 1. In Trial 18 the sharp rise is the transition between the photographic data and the results of the cloud envelope analysis. Thereafter $A/A_0\tau$ remains fairly constant at just under 2.2.

This may reflect an influence of atmospheric turbulent diffusion on the spreading of the cloud. Chatwin [14] has suggested that this can be represented by adding a term proportional to the friction velocity to the right-hand side of eqn. (1); he gives an analytical solution for the cloud radius. Con-

sideration of the order of magnitude of this diffusion term leads to the estimate that the area would attain twice the gravity-spreading value in a time $\tau \approx 4Ri_0$. For Trials 14 and 18, Ri_0 has values of 346 and 294 respectively [1] and so this may be a valid interpretation of the results in Fig. 8b. However, for Trial 15 with the lowest value of Ri_0 (219) the effect is not particularly marked.

The results for width-to-length ratios in Fig. 9 indicate that the length of clouds gradually approaches twice their width. For some of the low-Ri_0 trials (Fig. 9b) the ratio starts rising again. These are the trials for which the upwind edge of the cloud appears to move faster than the downwind edge: as discussed above this may be an effect of the sensitivity of the instruments.

3.5 Conclusions

The main conclusion to be drawn from this Section is that on the whole the estimates of area do not diverge significantly from the gravity-spreading law found to describe very well the early phases of each trial.

However, it appears that lateral turbulent diffusion may be necessary to explain better the results of low-Ri_0 trials. The amount of elongation of the clouds implies that the assumption of a circular cloud for modelling purposes may well be adequate since length and width are generally within 25% of the diameter of the equivalent circle.

4. Concluding remarks

In Section 2 we found that the photographic analysis of overhead views of the Thorney Island heavy gas dispersion trials gives strong support to the gravity-spreading equation (1) already used in many box models. The best estimate of the frontal Froude number, K, is 1.05. Since the photographic analysis can be applied only to the initial stages of each trial, we have sought to extend the results for area and position to much greater times by means of the cloud envelope analysis of Section 3. This procedure cannot give precise results because of the limitations imposed by the spacing and the sensitivity of the gas sensors and, presumably, because of the irregular nature of the real cloud outline. However, it does appear that the gravity-spreading equation continues to give an adequate prediction of the cloud area, although effects of atmospheric turbulent diffusion may be significant in some trials. Also the clouds become somewhat elongated, presumably because of the influence of the shear in the oncoming velocity profile.

While the cloud envelope analysis was intended to generate estimates of the boundary of the cloud, this amounts in practice to determination of the contour of the lowest detectable concentration. It could be adapted to estimating contours of higher concentrations by basing the envelopes on sensors that detected gas above the desired concentration and by using the times of arrival and departure of gas at that concentration. Thus the method is an alternative to traditional ways of drawing contours. At the outset of the

present work, we believed that trying to draw contours from the pattern of concentrations at a specific moment would be difficult due to the size of the mast spacing relative to the clouds and the fluctuating nature of the concentration records, so that contours might vary erratically from second to second. However Gotaas [15] and Hartwig [16] have now produced examples of such contours. Comparison with the present results will be interesting.

Acknowledgements

We would like to thank Dr. E. Brighton for helpful suggestions. The work reported in this paper was performed on behalf of the Health and Safety Executive and we would like particularly to thank Dr. J. McQuaid for his co-operation and encouragement. However, the views expressed here are those of the authors and do not necessarily reflect the views or the policy of the Health and Safety Executive.

References

1 P.W.M. Brighton, Area-averaged concentrations, height-scales and mass balances, J. Hazardous Materials, 11 (1985) 189—208.
2 L.S. Fryer and G.D. Kaiser, DENZ — a computer program for the calculation of the dispersion of dense toxic or explosive gases in the atmosphere, UKAEA Report SRD R152, 1979.
3 D.M. Webber, The physics of heavy gas clouds, UKAEA Report SRD R243, 1983.
4 A.J. Prince, D.M. Webber and P.W.M. Brighton, Thorney Island Heavy Gas Dispersion Trials — determination of path and area of cloud from photographs, UKAEA Report SRD R318, 1985.
5 P.W.M. Brighton, Using concentration data to track clouds in the Thorney Island experiments, UKAEA Report, 1985 (in press).
6 R.G. Picknett, Dispersion of dense gas puffs released in the atmosphere at ground level, Atm. Environ., 15 (1981) 509—525.
7 D.J. Hall, E.J. Hollis and H. Ishaq, A wind tunnel model of the Porton dense gas spill field trials, Warren Spring Laboratory Report LR394 (AP), 1982.
8 J.W. Rottman, J.C.R. Hunt and A. Mercer, The initial and gravity-spreading phases of heavy gas dispersion: comparison of models with Phase I data, J. Hazardous Materials, 11 (1985) 261—279.
9 B. Roebuck, The presentation and availability of the data and plans for future analysis, J. Hazardous Materials, 11 (1985) 373—380.
10 A.P. van Ulden, On the spreading of a heavy gas released near the ground, in: C.H. Buschmann (Ed.), Proc. 1st Int. Symp. on Loss Prevention and Safety Promotion in the Process Industries, The Netherlands, 1974, Elsevier, Amsterdam, 1974, pp. 221—226.
11 G.K. Batchelor, Diffusion from sources in a turbulent boundary layer, Arch. Mech. Stosow., 16 (1964) 661—670.
12 P.C. Chatwin, The dispersion of a puff of contaminant in the constant stress region, Quart. J. Roy. Meteorol. Soc., 94 (1968) 350—360.
13 M.J. Leck and D.J. Lowe, Development and performance of the gas sensor system, J. Hazardous Materials, 11 (1985) 65—89.

14 P.C. Chatwin, The incorporation of wind shear effects into box models of heavy gas dispersion, Report to the Health and Safety Executive under Contract No 1189.1/01.01, 1983.
15 Y. Gotaas, Heavy gas dispersion and environmental conditions as revealed by the Thorney Island experiments, J. Hazardous Materials, 11 (1985) 399—408.
16 S. Hartwig, Improved understanding of heavy gas dispersion due to the analysis of the Thorney Island trials data, J. Hazardous Materials, 11 (1985) 417—423.